

Atomic Layer MoS₂-Graphene van der Waals Heterostructure Nanomechanical Resonators

Fan Ye, Jaesung Lee, Philip X.-L. Feng*

*Department of Electrical Engineering & Computer Science, Case School of Engineering,
Case Western Reserve University, 10900 Euclid Avenue, Cleveland, OH 44106, USA*

Abstract

Heterostructures play significant roles in modern semiconductor devices and micro/nanosystems in a plethora of applications in electronics, optoelectronics, and transducers. While state-of-the-art heterostructures often involve stacks of crystalline epilayers each down to a few nanometers thick, the intriguing limit would be hetero-atomic-layer structures. Here we report the first experimental demonstration of freestanding van der Waals heterostructures and their functional nanomechanical devices. By stacking single-layer (1L) MoS₂ on top of suspended single-, bi-, tri- and four-layer (1L to 4L) graphene sheets, we realize array of MoS₂-graphene heterostructures with varying thickness and size. These heterostructures all exhibit robust nanomechanical resonances in the very high frequency (VHF) band (up to ~100 MHz). We observe that fundamental-mode resonance frequencies of the heterostructure devices fall between the values of graphene and MoS₂ devices. Quality (*Q*) factors of heterostructure resonators are lower than those of graphene but comparable to those of MoS₂ devices, suggesting interface damping related to interlayer interactions in the van der Waals heterostructures. This study validates suspended atomic layer heterostructures as an effective device platform and opens opportunities for exploiting mechanically coupled effects and interlayer interactions in such devices.

*Corresponding Author. Email: philip.feng@case.edu.

Introduction

Heterostructures, often referring to stacks of thin films combining at least two materials with different band structures, are important building blocks in modern semiconductor devices and micro/nanosystems, especially in electronics, optoelectronics, and solid-state transducers. A basic working principle of heterostructures is to use ‘bandgap engineering’ for manipulating carriers, *e.g.*, electrons and photons at interfaces, by leveraging the offsets in bandgaps of different constitutive materials. In electronic domain, elementary components such as p-n junctions and various diodes (including light emitting diodes (LEDs) [1] and solar cells [2]) are realized by stacking p-type and n-type thin layers. In optoelectronic and photonic domains, quantum wells and superlattices with periodically sandwiched thin layers are key to enabling many innovative diode lasers [3]. In mechanical domain, a classical example of heterostructures is a bimorph [4] that consists of two active layers and one passive layer, which is indispensable for many electromechanical actuators and sensors. To realize high-performance heterostructured devices, clean and abrupt interfaces are distinctly important, which have conventionally required highly advanced thin film growing and deposition techniques, such as molecular beam epitaxy (MBE) and atomic layer deposition (ALD). These have played significant roles and witnessed great successes and advances in creating state-of-the-art heterostructures in modern devices and technologies, attaining constitutive layers as thin as 9nm for selected materials (*e.g.*, Si/Ge, by MBE) [5].

The advent of atomically thin layered crystals and two-dimensional (2D) semiconductors (from graphene to transition metal dichalcogenides, *i.e.*, TMDCs) [6, 7, 8] offers new exciting opportunities for adding innovative members into the families of heterostructures, and new approaches to revolutionizing heterostructure devices, down to the ultimate limits of both discrete atomic layers and sharp hetero-interfaces. Enabled by atomic layer crystals, one can take a single-layer 2D material and stacking it on top of another single-layer 2D material. Distinct from traditional heterostructures that rely on strong chemical bonds between adjacent hetero-layers, such as ionic bonds and covalent bonds, the new atomically thin heterostructures are held together by van der Waal interactions [9]. Compared with devices made of individual 2D materials, van der Waals heterostructure devices demonstrate significant versatility and advantage in functions and performance, thus offering plentiful opportunities in both fundamental studies and device applications. For example, using atomic layers of h-BN as substrate, heterostructured graphene [10,11] and MoS₂ [12] FETs have been demonstrated with over tenfold mobility enhancement, with remarkable stability even under harsh conditions (high humidity and elevated temperature up to 500K) [13]. This mobility enhancement further allows the observation of Coulomb drag [14] and fractal quantum Hall effects [15], which has been elusive for devices with conventional SiO₂ insulator. In 2D heterostructure photovoltaics, the most studied are p-n junctions fabricated by combining p-type and n-type 2D semiconductor, *e.g.*, WSe₂/MoS₂ [16] junctions that show external quantum efficiency (EQE) from 10% to 30% with varying thickness [17]. In addition, phototransistors based on graphene/TMDCs/graphene structure exhibit extremely high EQE up to 30% [18]. Generally, two major approaches have been demonstrated for realizing van der Waals heterostructures: mechanical assembly including both solvent-assistant methods [10,19,20,21] and all-dry transfer techniques [22], epitaxy [16] or chemical vapor deposition (CVD) methods [23]. In comparison, mechanical assembly enables us to fabricate devices with high efficiency while CVD or epitaxy methods can achieve large scale heterostructures with finely controlled orientations between different layers.

Though important efforts have been made in van der Waals heterostructure devices, freestanding heterostructures of 2D crystals that possess mechanical degrees of freedom and controllable mechanical functions (such as bimorph) have not been explored yet. In this work, we describe the first experimental demonstration of suspended heterostructures enabled by atomic layer crystals (MoS₂ on graphene) with varying thickness, and the first nanomechanical resonators based on these freestanding heterostructures. We fabricate single-layer MoS₂ on single-layer graphene (1LMoS₂-1LGr), 1LMoS₂-2LGr, 1LMoS₂-3LGr and 1LMoS₂-4LGr (here Gr stands for graphene) heterostructure resonators, in circular drumhead geometry with various diameters. We find all these heterostructure devices exhibit robust nanomechanical resonances, up to ~100MHz in the very-high frequency (VHF) band. To systematically investigate resonance properties of the heterostructures, a set of control experiments of studying MoS₂ and graphene resonance properties are also performed. We find that fundamental resonance frequencies of the heterostructures always fall between those of their MoS₂ and graphene counterparts. In contrast, quality (Q) factors of heterostructure resonators are comparable to those of MoS₂ devices, but lower than those of graphene devices, implying an interlayer damping at the MoS₂-graphene interface. Finally, tension levels of heterostructure resonators are quantified by matching experimental data with theoretical calculations. These results provide evidence and initial insights for understanding interlayer interactions, and demonstrate a new platform for studying thermal properties and interlayer heat transfer of van der Waals heterostructures.

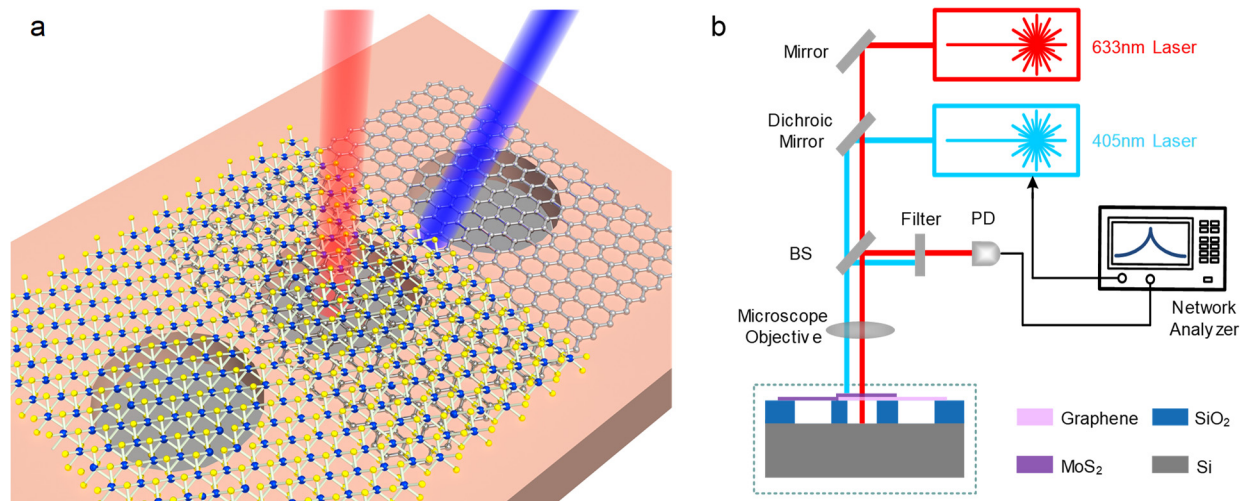


Figure 1: (a) Illustration of freestanding van der Waals heterostructures of MoS₂-graphene atomic layers. Blue, yellow and silver spheres represent Mo, S and C atoms, respectively. (b) Schematic of the nanomechanical resonance interferometry measurement system. A 405nm blue laser is employed to excite the resonance motion, and a 633nm red laser is used for motion detection. PD and BS represent photodetector and beam splitter, respectively. All measurements are performed in moderate vacuum (~20mTorr) at room temperature.

Results and Discussions

The fabrication of MoS₂-graphene heterostructure resonators starts from exfoliating graphene on SiO₂-on-Si substrates with pre-patterned arrays of microtrenches. After obtaining atomically thin graphene, single-layer (1L) MoS₂ flakes are transferred on top of the existing graphene flakes using an all-dry transfer method with alignment [22]. CVD MoS₂ layers are used in 1LMoS₂-1LGr, 1LMoS₂-2LGr and 1LMoS₂-3LGr devices, while exfoliated MoS₂ flakes are used in making

1LMoS₂-4LGr devices. The 1LMoS₂-1LGr van der Waals heterostructure is illustrated in **Figure 1a**. To study how the nanomechanical resonance characteristics of heterostructure are affected by the constituting MoS₂ and graphene layers, only part of graphene sheet is covered by MoS₂, for clear control experiments. As shown in Fig. 1b, an intensity-modulated 405nm blue laser is employed to excite the resonance and a 633nm red laser is focused at the center of the suspended region of the device, to detect motion by exploiting ultrasensitive interferometry techniques. To reduce air damping, devices are preserved in vacuum during measurement.

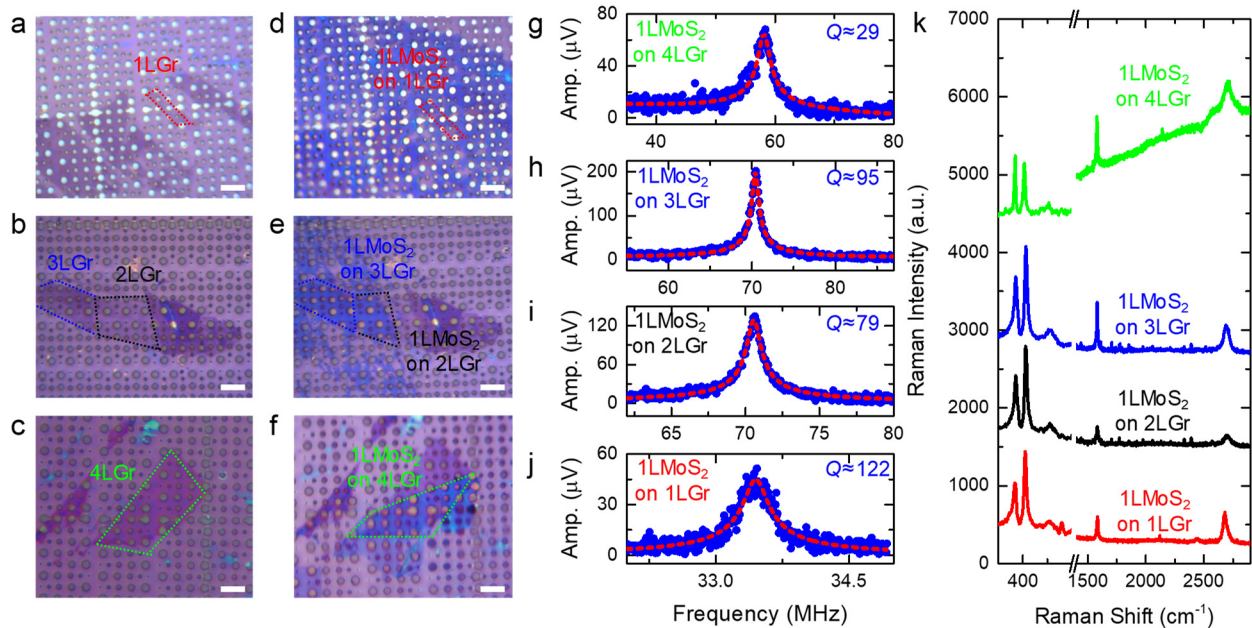


Figure 2: Microscopy images of (a) single-, (b) bi-, tri-, and (c) four-layer (1L to 4L) graphene flakes on substrates with arrays of circular microtrenches. Microscopy images of (d) 1LMoS₂ on 1LGr, (e) 1LMoS₂ on 2LGr, 1LMoS₂ on 3LGr, and (f) 1LMoS₂ on 4LGr suspended van der Waals heterostructures (here Gr stands for graphene) (Scale bar: 5 μ m). Fundamental-mode of one (g) 1LMoS₂ on 4LGr, (h) 1LMoS₂ on 3LGr, (i) 1LMoS₂ on 2LGr, and (j) 1LMoS₂ on 1LGr nanomechanical resonator. (k) Raman spectra of MoS₂-graphene heterostructure nanomechanical resonators.

Microscope images of 1L to 4L graphene nanosheets are shown in **Figure 2a** to **c**; and the corresponding heterostructure devices are illustrated in Fig. 2d to 2f. CVD MoS₂ flakes are used on top of 1L, 2L and 3L graphene while exfoliated MoS₂ is used on top of 4L graphene. As a result, we have attained totally 39 heterostructure devices, which facilitate us to study the statistics of the resonance characteristics. Figure 2g to 2j show the fundamental-mode resonances of devices of 1LMoS₂-4LGr, 1LMoS₂-3LGr, 1LMoS₂-2LGr and 1LMoS₂-1LGr, respectively. The measured resonance spectra are fitted to a damped simple harmonic resonator model to extract the fundamental-mode resonance frequency (f_0) and quality (Q) factor. The numbers of layers of the graphene and MoS₂ flakes are confirmed by Raman spectroscopy (Fig. 2k). The separation between E_{2g}¹ and A_{1g} peaks in MoS₂ is around 18.5cm⁻¹ for exfoliated sample and 20.8cm⁻¹ for CVD sample, indicating that the MoS₂ flakes are 1L [24]. The number of graphene layers is identified by the ratio of peak intensities between G mode and 2D mode. In 1L graphene, G peak is lower than 2D peak. In 2L graphene, the intensities of G mode and 2D mode are almost the same. In 3L graphene, G peak is slightly stronger than 2D peak. The peak intensity difference between G mode and 2D mode becomes larger in 4L graphene [25].

Statistical results of resonance frequencies and Q factors of 1LMoS₂-2LGr, 1LMoS₂-3LGr, and 1LMoS₂-4LGr circular drumhead devices with different diameters are shown in **Table S1** in **Supplementary Information**. The fundamental-mode resonances of most of the devices are in the VHF band, with the highest frequency reaching ~ 100 MHz. Interestingly, no clear size dependence of resonance frequency is observed in these devices, which could be attributed to different tension levels among these devices. The frequency versus Q factor plots are shown in **Fig. 3a**, **3b** and **3c** for 1LMoS₂-2LGr, 1LMoS₂-3LGr and 1LMoS₂-4LGr, respectively. The device with the highest figure-of-merit in each figure is highlighted by purple dash circle; the highest $f_0 \times Q$ obtained is 8.7×10^9 Hz in a 1LMoS₂-2LGr device.

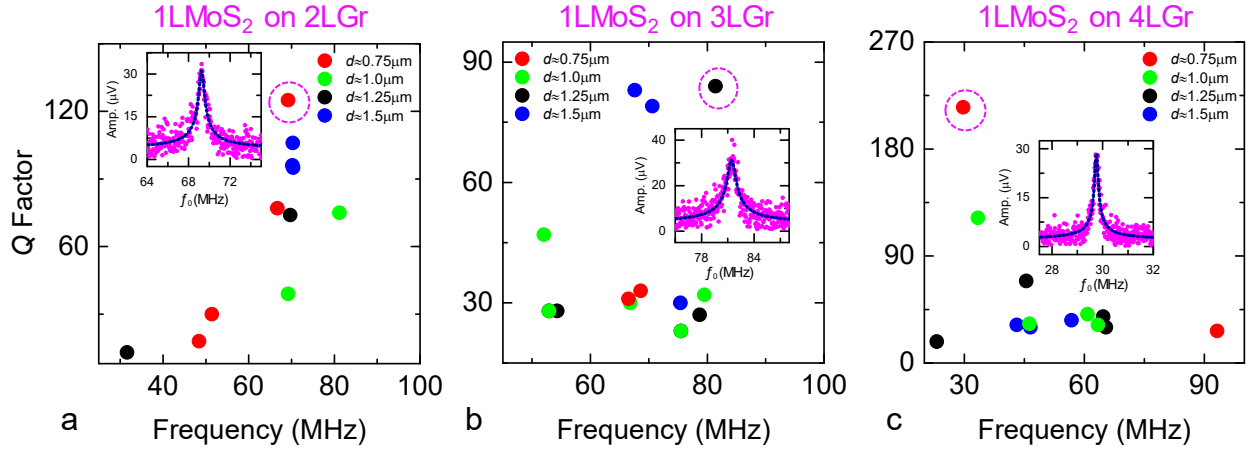


Figure 3: Fundamental-mode resonance frequency versus Q factor for (a) 1LMoS₂ on 2LGr, (b) 1LMoS₂ on 3LGr, and (c) 1LMoS₂ on 4LGr hetero-structure nanomechanical resonators. The highest $f_0 \times Q$ is highlighted by purple dashed circles. Inset in each panel: Resonances data and its fitting curve for the device having the highest $f_0 \times Q$ in its category.

We now turn to discuss differences on resonance properties among graphene, MoS₂, and resulting heterostructures. The frequencies and Q factors of 2L graphene, 1L MoS₂ and resulting 1LMoS₂-2LGr are shown in **Figure 4a** and **4d**. Generally, for devices of the same size (diameter), frequencies of heterostructure are higher than MoS₂ but lower than graphene. Similar trends are also observed in 1LMoS₂-3LGr (Fig. 4b) and 1LMoS₂-4LGr (Fig. 4c). By assuming the devices are in membrane regime, where the frequency is governed by built-in tension, the fundamental-mode resonance is given by

$$f_0 = \frac{2.404}{\pi d} \sqrt{\frac{\gamma}{\rho_{2D}}}, \quad (1)$$

where d is device diameter, ρ_{2D} is the areal mass density and γ is built-in tension. For 2L graphene, 1L MoS₂ and 1LMoS₂-2LGr heterostructures devices, if we assume that graphene, MoS₂ and heterostructure have the same built-in tension level γ , since $\rho_{2D,2LGr} < \rho_{2D,1LMoS_2} < \rho_{2D,1LMoS_2-2LGr}$, we shall obtain $f_{2LGr} > f_{1LMoS_2} > f_{1LMoS_2-2LGr}$, which is not consistent well with our experimental results ($f_{2LGr} > f_{1LMoS_2-2LGr} > f_{1LMoS_2}$). This implies that the tension levels are different among the MoS₂, graphene, and the resulted heterostructures. Another interesting point is the Q factor difference among the graphene, MoS₂ and the heterostructured

devices. It is observed that graphene devices exhibit higher Q factors than those of their MoS₂ and heterostructure counterparts. Based on Q factor equation $Q = f / \Gamma_m$, the Q factor of graphene is indeed expected to be larger than that of MoS₂ (given the same diameter) assuming that Γ_m (damping rate) remains the same for graphene and MoS₂ drumheads of the same diameter and thickness. However, though heterostructure devices exhibit higher frequencies than their MoS₂ counterparts, Q factors of heterostructure devices are similar to, or even lower than, those of their MoS₂ counterparts. This suggests a possible increase of damping due to additional energy dissipation related to interlayer frictions at the MoS₂-graphene interface.

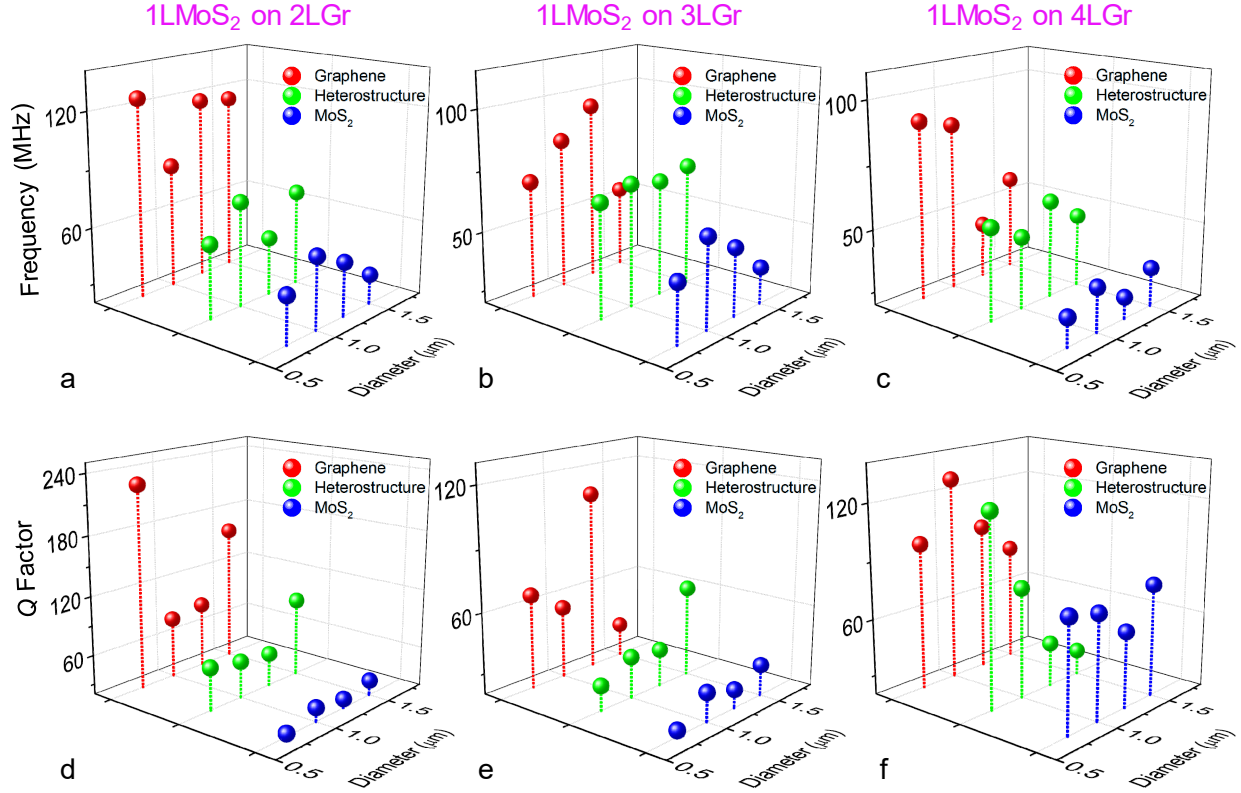


Figure 4: Comparison of the resonance frequencies measured from graphene, MoS₂ and their resulting heterostructures, for (a) 1L MoS₂ on 2L Gr, (b) 1L MoS₂ on 3L Gr, and (c) 1L MoS₂ on 4L Gr devices. Comparison of quality (Q) factors measured from graphene, MoS₂ and their resulting heterostructures in (d) 1L MoS₂ on 2L Gr, (e) 1L MoS₂ on 3L Gr, and (f) 1L MoS₂ on 4L Gr devices.

To further investigate the resonance frequency differences among the MoS₂, graphene, and the resulted heterostructures and probe their tension levels, analytical modeling is performed. The fundamental-mode resonance frequency of circular drumhead resonators can be expressed as [26,27]

$$f_0 = \left(\frac{k_m d}{4\pi} \right) \sqrt{\frac{16D}{\rho_{3D} t d^4} \left[\left(\frac{k d}{2} \right)^2 + \frac{\gamma d^2}{2D} \right]}, \quad (2)$$

where ρ_{3D} is the material mass density, t is device thickness, k_m is the modal parameter calculated numerically, γ refers to the built-in tension and D is the flexural rigidity, $D = E_Y t^3 / [12(1 - \nu^2)]$, in which E_Y and ν are Young's modulus and Poisson's ratio, respectively. As $\gamma d^2 / D \rightarrow \infty$, Eq. (2) approaches a membrane model, in which frequency is dominated by built-in tension. As $\gamma d^2 / D \rightarrow 0$, Eq. (2) approaches a plate model, in which frequency is dominated by Young's modulus E_Y . For heterostructures devices, Young's modulus and mass density vary as thickness changes. In our experiment, the MoS₂ thickness is fixed while graphene thickness increases from 1L to 4L, which gives us thickness of heterostructure as

$$t_{\text{hetero}} = t_{\text{Gr}} + 0.65\text{nm}, \quad (3)$$

where 0.65nm is single-layer MoS₂ thickness. The Young's modulus of heterostructure is given by [28]

$$E_{Y,\text{hetero}} t_{\text{hetero}} = E_{Y,\text{Gr}} t_{\text{Gr}} + E_{Y,\text{MoS}_2} t_{Y,\text{MoS}_2}. \quad (4)$$

Combining Eq. (3) and Eq. (4), the Young's modulus of heterostructure is given by

$$E_{Y,\text{hetero}} = E_{Y,\text{Gr}} - (E_{Y,\text{Gr}} - E_{Y,\text{MoS}_2}) \frac{0.65\text{nm}}{t_{\text{Gr}} + 0.65\text{nm}}. \quad (5)$$

Similar, mass density of heterostructure is given by

$$\rho_{\text{hetero}} t_{\text{hetero}} = \rho_{\text{Gr}} t_{\text{Gr}} + \rho_{\text{MoS}_2} t_{\text{MoS}_2}, \quad (6)$$

and combining Eq. (4) and Eq. (6), the mass density of heterostructure is given by

$$\rho_{\text{hetero}} = \rho_{\text{Gr}} - (\rho_{\text{Gr}} - \rho_{\text{MoS}_2}) \frac{0.65\text{nm}}{t_{\text{Gr}} + 0.65\text{nm}}. \quad (7)$$

Combining Eq. (2), Eq. (5) and Eq. (7), the scaling curves of heterostructures with varying size are calculated and plotted, which are shown in **Figure 5**. To investigate how the frequency of heterostructure resonators is affected by MoS₂ and graphene, we also perform analytical model for MoS₂ and graphene using Eq. (3), also shown in Figure 5. We find that most devices in this work, including graphene, MoS₂ and heterostructures, are in the tension regime and transition regime, with tension levels between 0.05N/m to 0.5N/m. The frequency difference among graphene, MoS₂ and resulting heterostructures is mainly attributed to different tension levels: MoS₂ devices have lower tension levels compared with graphene and heterostructures, which is the main reason for MoS₂ resonators exhibiting the lowest frequency and heterostructures in the middle. Similar trends are also observed in devices of other sizes (Fig. 5b to 5d). This tension difference between MoS₂ and graphene could be explained by different sealing conditions caused by different fabrication methods. The graphene resonators are fabricated by direct exfoliation, which result in a relatively tight contact between flakes and substrates. As a result, air molecules trapped in the cavity cannot escape in a short term. When devices are preserved in vacuum conditions, air bulging effects lead to a higher tension levels hence higher fundamental-mode frequencies. In comparison, MoS₂ devices are fabricated using all dry-transfer method. Thus, the contact between MoS₂ flakes and substrates are not as tight as graphene flakes with substrates. As a result, air in cavity leak quickly when devices are in vacuum chamber, leading to lower tension levels and frequencies [29]. Based on the aforementioned discussions and experimental results, it can be concluded that resonance of

heterostructure is dominated by bottom layer and affected by top layer, and an empirical equation describing the tension level could be expressed as,

$$\gamma_{\text{hetero}} = \gamma_{\text{top}} + \alpha\gamma_{\text{bottom}}, \quad (8)$$

where γ_{hetero} , γ_{top} and γ_{bottom} refer to the tension level of heterostructure, top layer and bottom layer respectively. The ‘‘interlayer coefficient’’ α describes how the tension level of heterostructure affected by bottom layer, which mainly depends on interface friction between top layer and bottom layer.

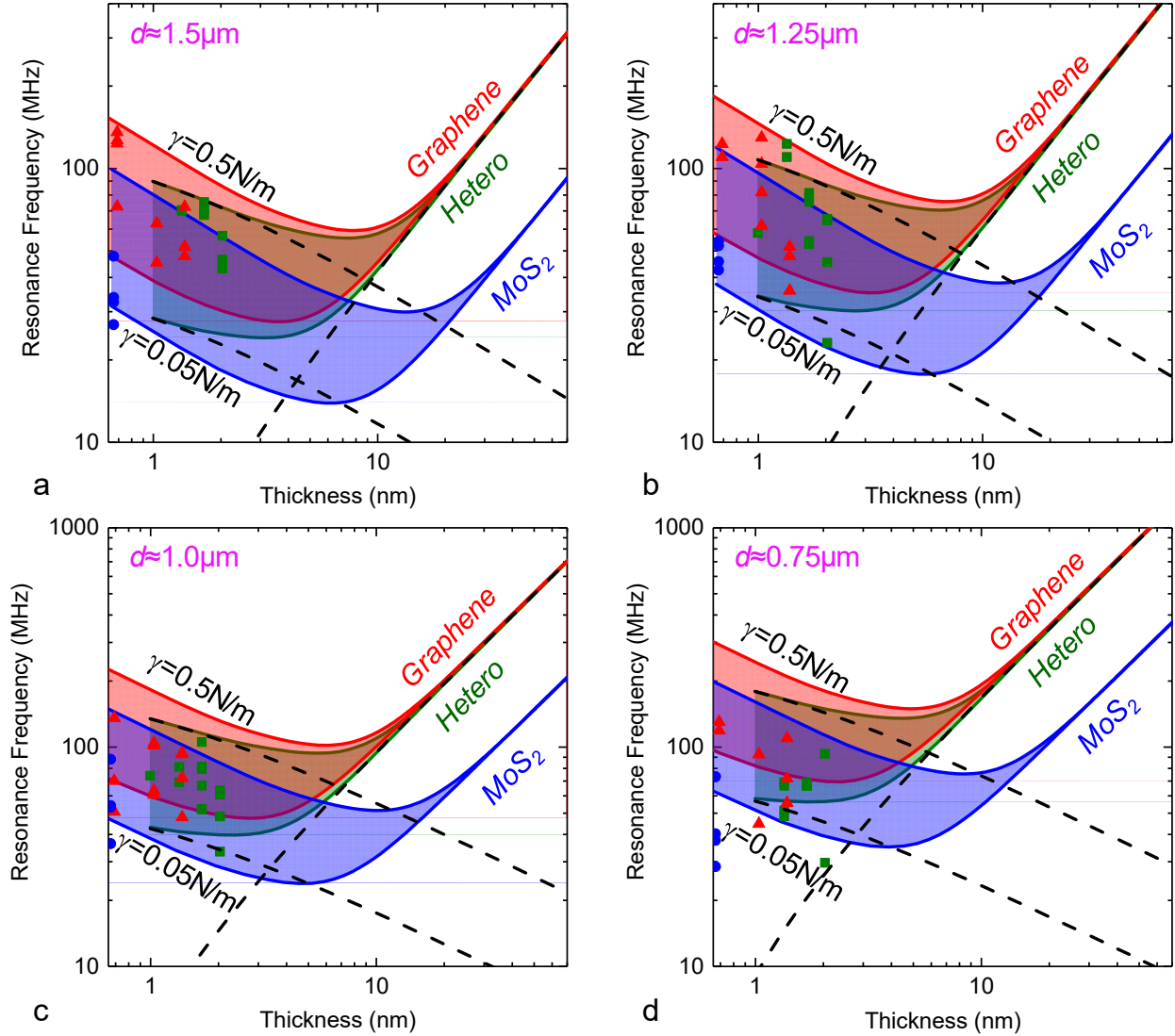


Figure 5: Frequency scaling of MoS₂-graphene van der Waals heterostructures for device diameters of (a) 1.5μm, (b) 1.25μm, (c) 1.0μm, and (d) 0.75μm. For each color, the upper solid line represents the calculated resonance frequency with a tension level of $\gamma = 0.5\text{N/m}$ and the lower one of $\gamma = 0.05\text{N/m}$. The shadowed region shows the range of tension levels between 0.05N/m and 0.5N/m. Dashed lines illustrate the ‘membrane’ and ‘disk’ limits of elastic behavior. Squares, triangles, and circles (in colors consistent with those of the corresponding curves) represent measured data from heterostructure, graphene, and MoS₂ devices, respectively.

As the thickness of device increases, the frequency is determined by combination of Young's modulus and tension, which is a transition regime between tension model and plate model. Compared with MoS₂ and graphene, heterostructure devices enter the transition regime with even the smallest possible thickness. For diameter of 0.75 μm and tension level of 0.05 N/m (Fig. 5d), even the thinnest heterostructure devices, 1LGr-1LMoS₂, are already in transition regime, implying a depletion of tension regime. For heterostructure devices in plate regime, the frequencies are the same as those of the graphene devices. This is because, for thick devices, from Eq. (5), the Young's modulus of the heterostructures is mainly determined by the Young's modulus of graphene.

Conclusions

In conclusion, we have demonstrated, for the first time, freestanding atomic layer MoS₂-on-graphene van der Waals heterostructures, based on which we have further realized nanomechanical resonators. All heterostructure devices exhibit robust resonances up to ~100 MHz in the VHF band, with figure-of-merit as high as $f_0 \times Q \approx 8.7 \times 10^9$ Hz. We observe high uniformity in the resonance frequencies and Q factors measured from these heterostructure resonators. The resonance frequencies and Q factors of the heterostructure devices are found to be in the middle (a compromise) between those of the devices based on a single constituting crystal (graphene or MoS₂). The measurement and analysis suggest that interlayer interactions play an important role in setting the tension level and damping of heterostructured resonators. This study not only opens new opportunities for studying multiphysical coupling effects in hetero-atomic-layer and bimorph 2D devices, but also sheds light on engineering mechanical degrees of freedom and interlayer interactions in van der Waals heterostructures.

Methods

Suspended MoS₂-Graphene Heterostructure Device Fabrication

The fabrication of MoS₂-graphene heterostructures and prototype bimorph devices starts from exfoliating graphene on SiO₂-on-Si substrates with pre-patterned arrays of microtrenches. After obtaining atomically thin graphene, single-layer (1L) MoS₂ flakes are carefully selected and transferred on top of the graphene flakes, by using an all-dry transfer method with alignment [22]. CVD MoS₂ layers are used in 1LMoS₂ on 1Lgraphene (Gr), 1LMoS₂ on 2LGr, and 1LMoS₂ on 3LGr devices, while exfoliated MoS₂ flakes are used in making 1LMoS₂ on 4LGr devices.

Raman Scattering Measurement

Heterostructure devices are preserved in a vacuum chamber and measured using customized micro-Raman system that is integrated into an optical interferometric resonance measurement system (please see the section below). The 532nm laser is focused on the center of the heterostructure device with a typical spot size around $\sim 1\mu\text{m}$ and laser power below $200\mu\text{W}$, to avoid excessive laser heating. Raman scattered light from the sample is collected in backscattering geometry and then guided to a spectrometer (Horiba iHR550) with a grating of 2400 g per mm. Raman signal is recorded using a liquid-nitrogen-cooled CCD. The spectral resolution of this system is $\sim 1\text{cm}^{-1}$.

Interferometric Resonance Measurement

We study MoS₂-graphene heterostructure devices and their nanomechanical resonances using an ultrasensitive laser interferometry system (Fig. 1b). The resonant motion is photothermally excited by using an amplitude modulated 405nm blue laser. To avoid excessive laser heating, laser is focused $\sim 5\mu\text{m}$ away from the devices with laser power below $300\mu\text{W}$. A network analyzer is used to control the modulation depth and frequency for modulating the 405nm laser, sweeping from 1MHz to 150MHz. The resonance motion is detected by a 633nm red laser with average power of $600\mu\text{W}$. Typical laser spot sizes are $\sim 5\mu\text{m}$ and $\sim 1\mu\text{m}$ for the 405nm and 633nm lasers, respectively. The output signal in the frequency domain is recorded by the same network analyzer.

Acknowledgement: We thank the financial support from National Science Foundation CAREER Award (Grant ECCS-1454570) and CCSS Award (Grant ECCS-1509721). Part of the device fabrication was performed at the Cornell NanoScale Science and Technology Facility (CNF), a member of the National Nanotechnology Infrastructure Network (NNIN), supported by the National Science Foundation (Grant ECCS-0335765).

Reference

- 1 S. Nakamura, T. Mukai and M. Senoh, *Jpn. J. Appl. Phys.*, 1991, **30**, 1998-2001.
- 2 A. Mittiga, E. Salza, F. Sarto, M. Tucci and R. Vasanthi, *Appl. Phys. Lett.*, 2006, **88**, 163502.
- 3 S. Nakamura, M. Senoh, S. Nagahama, N. Iwasa, T. Yamada, T. Matsushita, H. Kiyoku and Y. Sugimoto, *Jpn. J. Appl. Phys.*, 1991, **65**, 217-220.
- 4 G. Liu, Y. Zhang, P. Ci, and S. Dong, *J. Appl. Phys.*, 2013, **114**, 64107.
- 5 M. Sharma, M. K. Sanyal, M. K. Mukhopadhyay, M. K. Bera, B. Saha and P. Chakraborty, *J. Appl. Phys.*, 2011, **110**, 102204.
- 6 K. S. Novoselov, A. K. Geim, S. V Morozov, D. Jiang, Y. Zhang, S. V Dubonos, I. V Grigorieva and A. A. Firsov, *Science*, 2004, **306**, 666-669.
- 7 B. Radisavljevic, A. Radenovic, J. Brivio, V. Giacometti and A. Kis, *Nat. Nanotechnol.*, 2011, **6**, 147-150.
- 8 L. Li, Y. Yu, G. Ye, Q. Ge, X. Ou, H. Wu, D. Feng, X. Chen and Y. Zhang, *Nat. Nanotechnol.*, 2014, **9**, 372-377.
- 9 A. K. Geim and I. V Grigorieva, *Nature*, 2013, **499**, 419-425.
- 10 C. R. Dean, A. F. Young, I. Meric, C. Lee., L. Wang, S. Sorgenfrei, K. Watanabe, T. Taniguchi, P. Kim, K. L. Shepard and J. Hone, *Nat. Nanotechnol.*, 2010, **5**, 722-726.
- 11 L. Wang, I. Meric, P. Y. Huang, Q. Gao, Y. Gao, H. Tran, T. Taniguchi, K. Watanabe, L. M. Campos, D. A. Muller, J. Guo, P. Kim, J. Hone, K. L. Shepard and C. R. Dean, *Science*, 2013, **342**, 614-617.
- 12 X. Cui, G. H. Lee, Y. D. Kim, G. Arefe, P. Y. Huang, C. Lee, D. A. Chenet, X. Zhang, L. Wang, F. Ye, F. Pizzocchero, B. S. Jessen, K. Watanabe, T. Taniguchi, D. A. Muller, T. Low, P. Kim and J. Hone, *Nat. Nanotechnol.*, 2015, **10**, 534-540.
- 13 G. H. Lee, X. Cui, Y. D. Kim, G. Arefe, X. Zhang, C. H. Lee, F. Ye, K. Watanabe, T. Taniguchi, P. Kim and J. Hone, *ACS Nano*, 2015, **9**, 7019-7026.
- 14 R. V Gorbachev, A. K. Geim, M. I. Katsnelson, K. S. Novoselov, T. Tudorovskiy, I. V Grigorieva, A. H. MacDonald, S. V Morozov, K. Watanabe, T. Taniguchi and L. A. Ponomarenko, *Nat. Phys.*, 2012, **8**, 896-901.
- 15 C. R. Dean, L. Wang, P. Maher, C. Forsythe, F. Ghahari, Y. Gao, J. Katoch, M. Ishigami, P. Moon, M. Koshino, T. Taniguchi, K. Watanabe, K. L. Shepard, J. Hone and P. Kim, *Nature*, 2013, **497**, 598-602.
- 16 M. Y. Li, Y. Shi, C. C. Cheng, L. S. Lu, Y. C. Lin, H. L. Tang, M. L. Tsai, C. W. Chu, K. H. Wei, J. H. He, W. H. Chang, K. Suenaga and L. J. Li, *Science*, 2015, **349**, 524-528.
- 17 C. H. Lee, G. H. Lee, A. M. van der Zande, W. Chen, Y. Li, M. Han, X. Cui, G. Arefe, C. Nuckolls, T. F. Heinz, J. Guo, J. Hone and P. Kim, *Nat. Nanotechnol.*, 2014, **9**, 676-681.
- 18 L. Britnell, R. M. Ribeiro, A. Eckmann, R. Jalil, B. D. Belle, A. Mishchenko, Y. J. Kim, R. V Gorbachev, T. Georgiou, S. V Morozov, A. N. Grigorenko, A. K. Geim, C. Casiraghi, A. H. C. Neto and K. S. Novoselov, *Science*, 2013, **340**, 1311-1314.
- 19 F. Pizzocchero, L. Gammelgaard, B. S. Jessen, J. M. Caridad, L. Wang, J. Hone, P. Bøggild and T. J. Booth, *Nat. Commun.*, 2016, **7**, 11894.
- 20 P. J. Zomer, M. H. D. Guimarães, J. C. Brant, N. Tombros and B. J. van Wees, *Appl. Phys. Lett.*, 2014, **105**, 13101.

- 21 A. S. Mayorov, R. V Gorbachev, S. V Morozov, L. Britnell, R. Jalil, L. A. Ponomarenko, P. Blake, K. S. Novoselov, K. Watanabe, T. Taniguchi and A. K. Geim, *Nano Lett.*, 2011, **11**, 2396–2399.
- 22 R. Yang, X. Zheng, Z. Wang, C. J. Miller and P X-L Feng, *J. Vac. Sci. Technol. B, Nanotechnol. Microelectron. Mater. Process. Meas. Phenom.*, 2014, **32**, 61203.
- 23 J. A. Robinson, *ACS Nano*, 2016 **10** 42–45.
- 24 H. Li, Q. Zhang, C. C. R. Yap, B. K. Tay, T. H. T. Edwin, A. Olivier and D. Baillargeat, *Adv. Funct. Mater.*, 2012, **22**, 1385–1390.
- 25 A. C. Ferrari, J. C. Meyer, V. Scardaci, C. Casiraghi, M. Lazzeri, F. Mauri, S. Piscanec, D. Jiang, K. S. Novoselov, S. Roth and A. K. Geim, *Phys. Rev. Lett.*, 2006, **97**, 187401.
- 26 J. Lee, Z. Wang, K. He, J. Shan and P. X.-L. Feng, *ACS Nano*, 2013, **7**, 6086–6091.
- 27 J. Lee, F. Ye, Z. Wang, R. Yang, J. Hu, Z. Mao, J. Wei and P. X.-L. Feng, *Nanoscale*, 2016, **8**, 7854–7860.
- 28 M. R. Begley, H. Bart-Smith, O. N. Scott, M. H. Jones and M. L. Reed, *J. Mech. Phys. Solids*, 2005, **53**, 2557–2578.
- 29 J. Lee, Z. Wang, K. He, J. Shan and P. X.-L. Feng, *Appl. Phys. Lett.*, 2014, **105**, 23104.

Atomic Layer MoS₂-Graphene van der Waals Heterostructure Nanomechanical Resonators

Fan Ye, Jaesung Lee, Philip X.-L. Feng*

*Department of Electrical Engineering & Computer Science, Case School of Engineering,
Case Western Reserve University, 10900 Euclid Avenue, Cleveland, OH 44106, USA*

Table S1: Frequency and Quality (Q) Factors of Atomic Layer Graphene, MoS₂ and Their Vertically Stacked Heterostructure Nanomechanical Resonators

1L MoS₂ / 2L Graphene Heterostructures

Diameter $d \approx 0.75\mu\text{m}$

Device #	2L Graphene		Device #	1L MoS ₂ (CVD)		Device #	Heterostructure	
	f (MHz)	Q Factor		f (MHz)	Q Factor		f (MHz)	Q Factor
1	119.1	181	1	28.5	18	1	51.4	30
2	130.2	270	2	40.2	18	2	48.4	18
			3	73.3	33	3	69.2	125
			4	37.9	24	4	66.7	77
Normal Distributed Mean Value	124.6±7.8	226±63		45.0±19.5	23±7		58.9±10.5	63±48

Diameter $d \approx 1.00\mu\text{m}$

Device #	2L Graphene		Device #	1L MoS ₂ (CVD)		Device #	Heterostructure	
	f (MHz)	Q Factor		f (MHz)	Q Factor		f (MHz)	Q Factor
1	50.7	22	1	36.3	28	1	69.2	39
2	135.8	123	2	88.0	19	2	81.2	75
3	70.2	97	3	54.1	39			
			4	53.2	51			
Normal Distributed Mean Value	85.4±44.8	81±51		57.9±51.7	34±14		75.2±8.5	57±25

*Corresponding Author. Email: philip.feng@case.edu

Diameter $d \approx 1.25\mu\text{m}$

Device #	2L Graphene		Device #	1L MoS ₂ (CVD)		Device #	Heterostructure	
	f (MHz)	Q Factor		f (MHz)	Q Factor		f (MHz)	Q Factor
1	123.0	89	1	45.7	30	1	31.6	13
2	110.1	82	2	54.2	26	2	69.7	94
			3	52.2	22			
			4	42.6	39			
Normal Distributed Mean Value	116.6±9.1	86±5		48.7±5.4	29±8		50.6±26.8	53±57

Diameter $d \approx 1.50\mu\text{m}$

Device #	2L Graphene		Device #	1L MoS ₂ (CVD)		Device #	Heterostructure	
	f (MHz)	Q Factor		f (MHz)	Q Factor		f (MHz)	Q Factor
1	135.6	185	1	47.8	24	1	70.4	95
2	126.7	173	2	26.9	29	2	70.3	106
3	72.6	89	3	33.8	44	3	70.2	96
4	123.3	183	4	32.5	44			
Normal Distributed Mean Value	114.6±28.4	158±46		35.3±9.3	35±10		70.3±0.1	99±6

1L MoS₂ / 3L Graphene Heterostructures

Diameter $d \approx 0.75\mu\text{m}$

Device #	3L Graphene		Device #	1L MoS ₂ (CVD)		Device #	Heterostructure	
	f (MHz)	Q Factor		f (MHz)	Q Factor		f (MHz)	Q Factor
1	44.7	16	1	28.5	18	1	66.5	31
2	92.6	116	2	40.2	18	2	68.6	33
			3	73.3	33			
			4	37.9	24			
Normal Distributed Mean Value	68.7±33.9	66±70		45.0±19.5	23±7		67.6±1.5	32±1

Diameter $d \approx 1.00\mu\text{m}$

Device #	3L Graphene		Device #	1L MoS ₂ (CVD)		Device #	Heterostructure	
	f (MHz)	Q Factor		f (MHz)	Q Factor		f (MHz)	Q Factor
1	60.6	12	1	36.3	28	1	52.0	47
2	102.0	29	2	88.0	19	2	52.2	29
3	63.1	52	3	54.1	39	3	105.2	62
4	104.2	127	4	53.2	51	4	66.8	30
						5	79.5	32
Normal Distributed Mean Value	82.5±23.9	55±51		57.9±51.7	34±14		71.1±22.2	40±14

Diameter $d \approx 1.25\mu\text{m}$

Device #	3L Graphene		Device #	1L MoS ₂ (CVD)		Device #	Heterostructure	
	f (MHz)	Q Factor		f (MHz)	Q Factor		f (MHz)	Q Factor
1	103.9	91	1	45.7	30	1	81.4	84
2	81.8	56	2	54.2	26	2	52.9	28
3	61.8	67	3	52.2	22	3	75.5	23
4	129.7	197	4	42.6	39	4	78.7	27
						5	54.3	28
Normal Distributed Mean Value	94.3±29.2	103±65		48.7±5.4	29±8		68.4±14.1	38±26

Diameter $d \approx 1.50\mu\text{m}$

Device #	3L Graphene		Device #	1L MoS ₂ (CVD)		Device #	Heterostructure	
	f (MHz)	Q Factor		f (MHz)	Q Factor		f (MHz)	Q Factor
1	45.3	19	1	47.8	24	1	67.6	83
2	63.0	53	2	26.9	29	2	70.6	79
			3	33.8	44	3	75.4	30
			4	32.5	44			
Normal Distributed Mean Value	54.2±12.5	36±24		35.3±9.3	35±10		71.2±3.9	64±30

1L MoS₂ / 4L Graphene Heterostructures

Diameter $d \approx 0.75\mu\text{m}$

Device #	4L Graphene		Device #	1L MoS ₂ (Exfoliated)		Device #	Heterostructure	
	f (MHz)	Q Factor		f (MHz)	Q Factor		f (MHz)	Q Factor
1	71.9	76	1	24.2	23	1	29.7	215
2	109.8	118	2	43.7	113	2	93.2	27
			3	14.2	9			
			4	27.6	76			
			5	47.2	174			
Normal Distributed Mean Value	90.5±26.2	97±30		31.4±13.8	79±67		61.5±44.9	121±96

Diameter $d \approx 1.00\mu\text{m}$

Device #	4L Graphene		Device #	1L MoS ₂ (Exfoliated)		Device #	Heterostructure	
	f (MHz)	Q Factor		f (MHz)	Q Factor		f (MHz)	Q Factor
1	72.3	45	1	33.6	104	1	33.4	122
2	92.8	132	2	42.5	95	2	63.4	32
3	93.9	203	3	31.4	37			
			4	31.9	31			
			5	29.6	35			
			6	46.5	71			
			7	43.9	154			
Normal Distributed Mean Value	86.3±12.2	127±79		37.5±7.0	75±46		48.4±21.2	77±64

Diameter $d \approx 1.25\mu\text{m}$

Device #	4L Graphene		Device #	1L MoS ₂ (Exfoliated)		Device #	Heterostructure	
	f (MHz)	Q Factor		f (MHz)	Q Factor		f (MHz)	Q Factor
1	35.8	122	1	17.1	114	1	45.5	69
2	47.9	74	2	25.3	52	2	65.4	30
			3	26.9	21	3	64.7	39
			4	26.6	44	4	23.1	18
			5	35.1	51			
			6	34.5	137			
			7	7.55	8			
			8	35.5	157			
Normal Distributed Mean Value	41.9±8.6	98±35		26.1±9.8	73±56		49.7±20.0	39±22

Diameter $d \approx 1.50\mu\text{m}$

Device #	4L Graphene		Device #	1L MoS ₂ (Exfoliated)		Device #	Heterostructure	
	f (MHz)	Q Factor		f (MHz)	Q Factor		f (MHz)	Q Factor
1	47.9	132	1	18.8	81	1	43.1	32
2	72.4	52	2	23.9	25	2	46.5	30
3	51.8	61	3	51.2	68	3	56.8	36
			4	23.2	82			
			5	66.1	16			
			6	28.9	203			
Normal Distributed Mean Value	57.4±13.2	82±44		35.3±18.9	79±67		48.8±7.1	33±3